A Simple Detection and Identification Scheme For Reconfigurable Intelligent Surfaces

Aymen Khaleel, Recep Vural, Mehmet Cagri Ilter, Majid Gerami, and Ertugrul Basar, *Fellow, IEEE*

***Abstract*—Reconfigurable intelligent surface (RIS)-empowered communication is one of the promising physical layer enabling technologies for the sixth generation (6G) wireless networks due to their unprecedented capabilities in shaping the wireless communication environment. RISs are modeled as passive objects that can not transmit or receive wireless signals. While the passiveness of these surfaces is a key advantage in terms of power consumption and implementation complexity, it limits their capability to interact with the other active components in the network. Specifically, unlike conventional base stations (BSs), which actively identify themselves to user equipment (UEs) by periodically sending pilot signals, RISs need to be detected from the UE side. This paper proposes a novel RIS identification (RIS-ID) scheme, enabling UEs to detect and uniquely identify RISs in their surrounding environment. Furthermore, to assess the proposed RIS-ID scheme, we propose two performance metrics: the false and miss detection probabilities. These probabilities are analytically derived and verified through computer simulations, revealing the effectiveness of the proposed RIS-ID scheme under different operating scenarios.**

***Index Terms*—Reconfigurable intelligent surfaces, sensing, detection, identification.**

I. Introduction

RECONFIGURABLE intelligent surfaces continue receiving growing attention as one of the game-changing physical layer enabling technologies in the sixth generation (6G) of wireless communications. RISs composed of dynamically controllable metamaterial elements, carries the potential to bring huge enhancements into wireless communication systems through its remarkable ability to exert unprecedented control over electromagnetic waves [1]. By manipulating the phase, amplitude, and polarization of signals, a RIS can enhance communication links, improve energy efficiency, and mitigate interference [2]. RISs have been studied and applied with various wireless communication contexts, including non-orthogonal multiple access (NOMA) [3], multiple-input multiple-output (MIMO) [4], index modulation [5], and beyond.

Additionally, RIS technology extends beyond information communication systems and finds utility in localization [6] and sensing [7]–[11] systems. For instance, In [7], the authors designed a radio-frequency (RF) sensing system leveraging RISs for human posture recognition where optimal RIS configuration is obtained to minimize posture recognition errors. In [8], the authors introduced hybrid RISs (HRISs), which not only reflect impinging signals but also incorporate active reception elements for sensing and processing. The findings indicate that HRISs enable more efficient channel estimation, requiring notably fewer pilots than fully reflective RISs. In [9], the authors investigated RIS-aided integrated sensing and communication (ISAC) within a multi-user multiple-input single-output (MISO) downlink communication system. The authors developed an algorithm for joint transmit beamforming and RIS configuration to maximize the sum-rate of multiple users while ensuring the minimum signal-to-noise ratio (SNR) required for effective target detection in the radar. The study of [10] incorporated NOMA technology into an RIS-assisted ISAC system, where the RIS was utilized to create a virtual line-of-sight (LoS) connection between the base station (BS) and both the communication users and radar targets. In [11], the authors investigated simultaneous transmitting and reflecting (STAR) RIS-aided ISAC system, that removes the necessity of communication users or radar targets to be positioned on the same side as the BS and RIS. In [12], a localization approach is introduced employing modulated RISs. Here, a BS transmits an unmodulated carrier signal, subsequently modulated by multiple RISs by applying phase shifts following an m-sequence. Signals from different RISs are distinguished thanks to their unique m-sequences and the use of a time division method to run a single RIS at a time. Finally, the user estimates its location using time-difference-of-arrival information from received signals. In [13], a study on BS-free RIS-aided localization is conducted. In the considered scenario, the UE estimates its location by transmitting orthogonal frequency-division multiplexing (OFDM) pilots and then analyzing the signals reflected from the RIS, whose location, position, and phase profile are known by the UE.

Considering the current cellular wireless networks, a BS identifies itself to user equipment (UEs) by periodically sending synchronization signals, where the task of the UE is to search and detect them [14]. Unlike a conventional BS, a RIS is a passive device that cannot transmit or receive wireless signals. In this sense, a RIS is a passive object (a group of scatterer) that cannot identify itself actively; instead, the network terminals (NTs), i.e., BS or UE, need to detect it. This can be extended to the scenario where multiple RISs are deployed in the environment, and in such cases, NTs need to detect and uniquely identify them; we refer to this as the *RIS identification (RIS-ID) process*. In analogy to a radar system, RIS-ID can be seen as an active sensing process,

Aymen Khaleel, Recep Vural, and Ertugrul Basar are with the Communications Research and Innovation Laboratory (CoreLab), Department of Electrical and Electronics Engineering, Koç University, Sariyer, Istanbul 36050, Turkey (e-mail: akhaleel@ku.edu.tr; rvural22@ku.edu.tr; ebasar@ku.edu.tr).

Mehmet Cagri Ilter is with the Department of Information and Communications Engineering, Aalto University, Espoo, Finland (e-mail: mehmet.ilter@aalto.fi).

Majid Gerami is with Huawei Technologies Sweden AB, Kista, Sweden (email: majid.gerami@huawei.com).

where the deployed RISs are the targets and the UE is the radar active transceiver. Consequently, it can be seen that the RIS-ID process is the first and most essential step to utilize an RIS.

To the best of the authors' knowledge, the RIS-ID problem has not yet been investigated in the literature. In this context, current literature implicitly consider that NTs are aware of the deployed RISs' existence, which is practically an invalid assumption. As a potential solution, one might argue that the geographical coordinates of deployed RISs can be shared as a look-up table by the wireless network with UEs. In this way, based on their current locations, UEs can identify nearby deployed RISs using the shared look-up table and thus utilize them. However, having a nearby RIS does not guarantee that the UE can have access to it due to blocking obstacles; this is more evident in indoor scenarios. Practically, the geographical coordinates of these obstacles can not be obtained nor included in the shared look-up table, which makes this solution limited.

In this study and in contrast to the previous background, we propose a novel RIS detection and identification scheme. Using the proposed scheme, an UE can actively sense the existence of an RIS in the environment and uniquely identify it among other deployed RISs. Specifically, the main contributions of this study can be summarized as follows.

- To the best of authors' knowledge, this is the first study in the literature to consider the RIS detection and identification problem. To tackle this problem, inspired by radar systems, we propose a novel active sensing scheme for UEs.
- In order to assess the proposed RIS-ID scheme, we derive the false and miss-detection probabilities as the main performance metrics.
- We provide a practical procedure to set the detection threshold at UE to achieve a targeted false and miss-detection probabilites.

The rest of the paper is organized as follows. Section II introduces the RIS-ID problem in cellular networks, followed by the system model of the proposed scheme. In Section III, we present the fundamental metrics used to evaluate the performance of the proposed scheme: false detection and miss-detection probabilities. Extensive computer simulations and performance analysis are provided in Section IV. Finally, Section V summarizes our findings and discusses potential future directions.

II. RIS Detection and Identification

In this section, we first describe the RIS-ID problem in a general cellular network. Afterward, we will move forward to more detailed system model and introduce the proposed solution for the RIS identification.

A. Problem Formulation

Fig. 1 shows a cellular network with multiple RISs deployed to assist the BS-UE communication. Specifically, in Fig. 1, RISs in black color are the ones out of the range of communication with respect to the UE, mainly due to the high path loss. In red color are the RISs within the range of communication but unreachable by the UE due to blocking obstacles. Finally, in green color are the RISs within the communication range and also reachable by the UE. The UE first establishes its connection with the BS and then, based on a rough estimate of the UE's current location[1], the BS sends the UE a look-up table of the potentially reachable RISs in its neighbor (the ones in red and green color). Using our proposed RIS-ID scheme, the UE employs an active sensing procedure (like a radar) to sense the reachable RISs (the green ones) using the shared look-up table. Following up the RIS-ID process, the UE can utilize the green RISs for various functions. In what follows, a detailed explanation of the RIS-ID scheme is presented.

B. Proposed RIS-ID Solution: System Model

Consider a full-duplex[2] single-antenna UE aims to detect and uniquely identify the nearby deployed RISs, as illustrated in Fig. 1. Each RIS has an ID number that is uniquely associated with its phase shift reflection pattern (PSRP), where the shared look-up table is used to link RISs IDs with their corresponding PSRPs. The RIS-ID process starts when the UE continuously transmits (omnidirectional) an unmodulated carrier signal and listens to the echoes simultaneously. Reachable RISs in the vicinity of the UE (green ones in Fig. 1) reflect the carrier signal back to the UE remodulated with their unique PSRPs[3]. At the UE side, the received signal is correlated with locally generated versions of the PSRPs given in the shared look-up table. Next, each PSRP with a correlation output higher than a predetermined detection threshold is mapped back to the corresponding RIS ID using the look-up table, declaring the detection of that RIS.

Let l (superscript) and m (subscript) denote the indices of the RIS and received symbol at the UE side, respectively. Accordingly, let $\mathbf{h}_{\text{UR},m}^{(l)}$ and $\mathbf{h}_{\text{RU},m}^{(l)} \in \mathbb{C}^{N^{(l)}\times 1}$, denote the UE-RIS and RIS-UE channels, respectively, where $N^{(l)}$ is the RIS size. Then, under the channel reciprocity assumption, we have $\mathbf{h}_{\text{UR},m}^{(l)} = \mathbf{h}_{\text{RU},m}^{(l)} = \mathbf{h}_{m}^{(l)}$[4]. Considering spatially correlated Rayleigh fading channels, we have $\mathbf{h}_{m}^{(l)} \sim \mathcal{CN}(\mathbf{0}, P\beta^{(l)}\mathbf{R}), \forall l, m$, where $\mathcal{CN}(0,\sigma^2)$ stands for complex Gaussian distribution with zero mean and variance σ^2. Here, P is the transmit power, $\beta^{(l)}$ is the path gain, $\mathbf{0}$ denotes $N^{(l)}$-dimensional vector of zeros and $\mathbf{R} \in \mathbb{C}^{N^{(l)}\times N^{(l)}}$ denotes the RIS correlation matrix [16]. Also, $\mathbf{\Phi}_{m}^{(l)} \in \mathbb{C}^{N^{(l)}\times N^{(l)}}$ and $n_m \sim \mathcal{CN}(0,\sigma_n^2)$ denote the RIS phase shift matrix and the additive white Gaussian noise (AWGN) sample, respectively. Thus, when there are L potentially reachable RISs (green and red ones in Fig. 1) exist in the vicinity of UE (according to the shared look-up table), the received signal corresponding to the m-th reflected symbol can be expressed as[5]

[1]The BS can acquire this information using traditional received signal strength indicator (RSSI) ranging-based localization methods.

[2]Self-interference can be readily managed using traditional digital cancellation techniques [15].

[3]Here, without loss of generalization for the proposed scheme, we assume all of the RIS elements are continuously being adjusted for the purpose of RIS-ID, or possibly subsurface (partition) of them.

[4]Note that, all of the derivations in this study still hold for the scenario of non-reciprocal Rayleigh fading channels.

[5]Here, we consider that the propagation delays associated with different RISs are so small that the reflected symbols from all RISs reach the UE in approximately the same time, which is a reasonable assumption due to close proximity of UE-side RISs employed in the system.

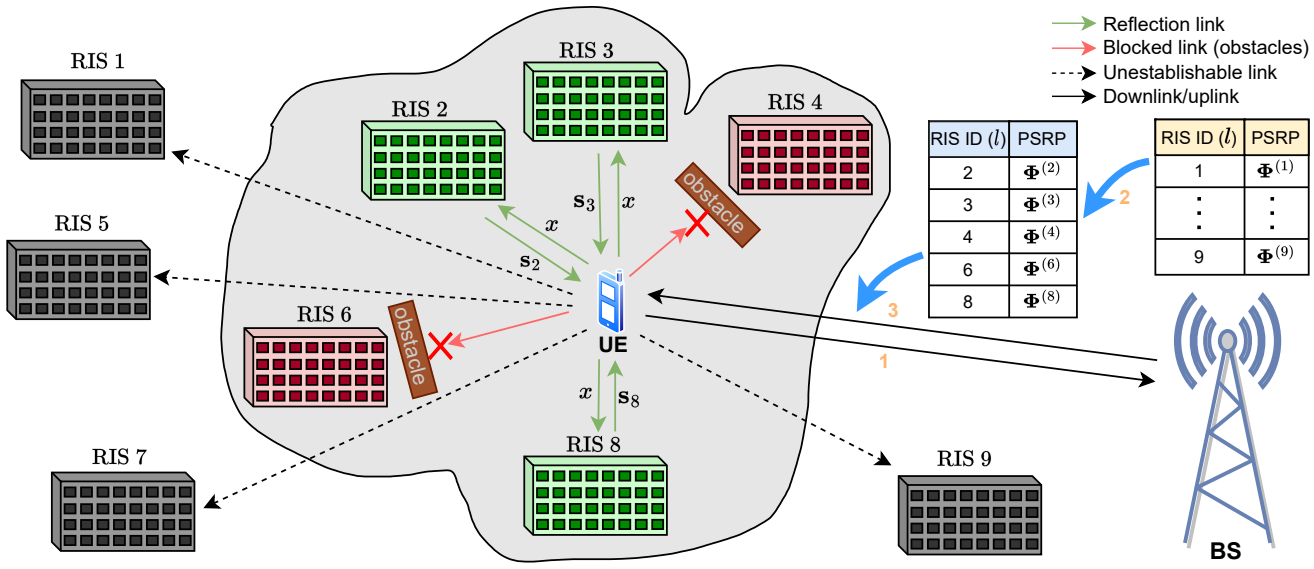

Fig. 1. An illustration of an RIS-assisted cellular wireless network where a UE tries to detect the existence of the RISs deployed in its surroundings and uniquely identify them. In this specific scenario, there are three reachable, two blocked, and four out-of-range RISs.

$$
\begin{aligned}
y_m &= x \sum_{l=1}^{L} \left[(\mathbf{h}_m^{(l)})^T \mathbf{\Phi}_m^{(l)} \mathbf{h}_m^{(l)} \right] \eta^{(l)} + n_m \\
&\overset{\text{I}}{=} x \sum_{l=1}^{L} e^{j\phi_m^{(l)}} \left[(\mathbf{h}_m^{(l)})^T \mathbb{I}_{N^{(l)}} \mathbf{h}_m^{(l)} \right] \eta^{(l)} + n_m \\
&\overset{\text{II}}{=} \sum_{l=1}^{L} e^{j\phi_m^{(l)}} \tilde{h}^{(l)} \eta^{(l)} + n_m \\
&= \sum_{l=1}^{L} \mathbf{s}_m^{(l)} \tilde{h}^{(l)} \eta^{(l)} + n_m, \qquad (1)
\end{aligned}
$$

where, $x = 1$ stands for the complex baseband sample corresponding to the passband transmission of unmodulated carrier signal $\cos(2\pi f_c t)$ with f_c is the operating frequency and t denotes time. Furthermore, in step I, corresponding to the PSRP, we set $\mathbf{\Phi}_m^{(l)} = e^{j\phi_m^{(l)}} \mathbb{I}_{N^{(l)}}$ with unity reflection amplitude, and $\mathbb{I}_{N^{(l)}}$ denotes an identity matrix with size $N^{(l)}$. In step II, considering that the channel coherence time is larger than the time required to receive all of the reflected symbols at UE[6], we drop the symbol index m and set $\tilde{h}^{(l)} = (\mathbf{h}^{(l)})^T \mathbb{I}_{N^{(l)}} \mathbf{h}^{(l)}$. Furthermore, $\mathbf{s}_m^{(l)} = e^{j\phi_m^{(l)}}$ denotes the m-th element of the PSRP vector $\mathbf{s}^{(l)}$ associated with the l-th RIS. Here, we use $\eta^{(l)} \in \{0, 1\}$ as a random variable (RV) that indicates if the l-th RIS is reachable ($\eta^{(l)} = 1$) or unreachable ($\eta^{(l)} = 0$), from the UE perspective.

Here, motivated by the work in [12], the PSRP of the RIS ($\mathbf{\Phi}_m^{(l)}$) is chosen to modulate x with binary phase shift keying (BPSK) symbols of a unique binary sequence (BSeq) vector $\mathbf{q}^{(l)}$, as follows. Independent from the UE, the RIS periodically adjusts its elements with a common phase shift that is applied to all of them. Specifically, at the reflection of the m-th symbol, the phase shift applied to x can be expressed as

$$
\phi_m^{(l)} = \frac{1}{j} \ln q_{\tilde{m}}^{(l)}, \; m, \tilde{m} \in \{1, 2, \ldots, M\}, \qquad (2)
$$

where $\tilde{m} = (c + m - 1) \mod M + 1$ is the index of the m-th BSeq symbol modulating x. Here, c is the index of the first BSeq symbol modulating x, where it is seen from the UE receiver side as a random integer number; we model it using the uniform distribution, $c \in \mathcal{U}\{1, 2, \ldots, M-1\}$. Furthermore, $q_{\tilde{m}}^{(l)}$ is the $\tilde{m}$-th element (symbol) of the BSeq vector $\mathbf{q}^{(l)} = [q_1^{(l)}, \cdots, q_M^{(l)}]$, $q_m^{(l)} \in \{0, 1\}$.

If there is no reachable RIS in its vicinity, the received signal at UE can be rewritten as

$$
y_m = n_m, \qquad (3)
$$

after interference from other RF sources is ignored.

Overall, at the UE side, the vector of the collected samples is given as

$$
\mathbf{y} = [y_1, \ldots, y_{v_1}, y_{v_1+1}, \ldots, y_{v_1+M}, \ldots, y_{v_1+M+v_2}], \qquad (4)
$$

where, v_1 and v_2 are the numbers of samples collected before and after the received reflections' samples of x from the L RISs, respectively, and they contain the AWGN samples only, where $y_1, \cdots, y_{v_1}, y_{v_1+M+1}, \cdots, y_{v_1+M+v_2} \sim \mathcal{CN}(0, \sigma_n^2)$, as in (3). Accordingly, the samples $y_{v_1+1}, \cdots, y_{v_1+M}$ correspond to the received signal samples, y_m's, which were already given in (1).

In light of the above, the detection process for the l-th RIS starts by generating the detected symbol [14]

$$
d_{c,k}^{(l)} = \frac{1}{\sqrt{M}} \sum_{m=1}^{M} \mathbf{s}_{c,m}^{(l)} \mathbf{y}_{m+k}, 0 \le k \le v_1 + v_2, \qquad (5)
$$

by letting $\mathbf{s}^{(l)}$ denoting the BPSK modulated sequence vector $\mathbf{q}^{(l)}$, we have $\mathbf{s}_{c,m}^{(l)} \in \{-1, 1\}$ corresponds to the $((c + m - 1) \mod M + 1)$-th element of the vector $\mathbf{s}^{(l)}$, or equivalently, the m-th element of the vector $\mathbf{s}^{(l)}$ with its elements are circularly shifted by c to the left. Also, $\mathbf{y}_{m+k}$ is the $(m+k)$-th element of $\mathbf{y}$. Note that the normalization factor $1/\sqrt{M}$ is used to reduce the overall noise variance resulting

[6]Another option, when the BSeq has a longer duration, is to correlate only a segment of the received signal such that the channel coherence time is still larger.

from the correlation process in case of no RIS, leading to significantly high false detection probability. Next, we obtain c and k associated with the maximum correlation amplitude as

$$(\hat{c},\hat{k})^{(l)} = \arg\max_{c,k} |d_{c,k}^{(l)}|^2. \tag{6}$$

Finally, from (6), we obtain our decision metric as

$$D^{(l)} = |d_{\hat{c},\hat{k}}^{(l)}|^2. \tag{7}$$

Consequently, an RIS detection is declared only when $D^{(l)} > r^{(l)}$, where $r^{(l)}$ is a predetermined threshold that will be discussed in the next section. Accordingly, from the UE perspective, the l-th RIS is said to be reachable only if $D^{(l)} > r^{(l)}$, irrespective of the geographical location of that RIS relative to the UE. Note that the estimation of propagation delay (and hence, v_1) can be obtained from $\hat{k}^{(l)}$ as it is done in [12], while here, we focus on the RIS detection identification only.

III. Performance Metrics of The RIS-ID Scheme

In this section, we provide two fundamental metrics to assess the performance of the proposed RIS-ID scheme. First, we derive the false detection probability $P_F^{(l)}$, which corresponds to the probability of declaring a detection ($\eta^{(l)}=1$) of the l-th RIS while it is unreachable ($\eta^{(l)}=0$). On the other side, we derive the miss detection probability $P_{miss}^{(l)}$ as the probability of declaring the l-th RIS unreachable ($\eta^{(l)}=0$) while it is reachable ($\eta^{(l)}=1$).

A. False Detection Probability

In light of the earlier introduction, the false detection probability for the l-th RIS can be written as

$$\begin{aligned}
P_F^{(l)} &= P(D^{(l)} > r^{(l)} | \eta^{(l)}=0) \\
&= P\Big(D^{(l)} > r^{(l)} \Big| \bigcap_{\substack{\tilde{l}=1 \\ \tilde{l}\neq l}}^{L-1} \eta^{(\tilde{l})}\Big) P\Big(\bigcap_{\substack{\tilde{l}=1 \\ \tilde{l}\neq l}}^{L-1} \eta^{(\tilde{l})}\Big) \\
&\overset{\text{I}}{=} \sum_{w=1}^{2^{L-1}} B^{(l)} P\Big(\bigcap_{\substack{\tilde{l}=1 \\ \tilde{l}\neq l}}^{L-1} (\eta^{(\tilde{l})} = \eta_w^{(\tilde{l})})\Big) \overset{\text{II}}{=} \sum_{w=1}^{2^{L-1}} B^{(l)} P\Big(\eta^{(\tilde{l})} = \eta_w^{(\tilde{l})}\Big) \\
&\overset{\text{III}}{=} \Big(\frac{1}{2}\Big)^{L-1} \sum_{w=1}^{2^{L-1}} B^{(l)},
\end{aligned} \tag{8}$$

where,

$$B^{(l)} = P\Big(D^{(l)} > r^{(l)} \Big| \bigcap_{\substack{\tilde{l}=1 \\ \tilde{l}\neq l}}^{L-1} (\eta^{(\tilde{l})} = \eta_w^{(\tilde{l})})\Big). \tag{9}$$

In step I of (8), we consider all of the possible combinations of potentially reachable/unreachable RISs given in the shared look-up table, where we have $w = 2^{L-2}\eta_w^{(L-1)} + 2^{L-3}\eta_w^{(L-2)} + \cdots + \eta_w^{(1)} + 1$ possibilities. Without loss of generality, in step II, we consider that the l-th RIS can be reachable/unreachable independent from the $\tilde{l}$-th RIS, $\forall l, \tilde{l} \in \{1,\ldots,L\}$, and in step III, an RIS is considered to be reachable or unreachable with the same probability[7].

In order to proceed, we need to find the right-tail probability associated with $D^{(l)}$, as follows. First, from (5), we expand $d_{c,k}^{(l)}$ as follows

$$\begin{aligned}
d_{c,k}^{(l)} &= \frac{1}{\sqrt{M}} \sum_{m=1}^{M} \mathbf{s}_{c,m}^{(l)} \mathbf{y}_{m+k} \\
&\overset{\text{I}}{=} \frac{1}{\sqrt{M}} \left[\sum_{m_1=1}^{v_1-k} \mathbf{s}_{c,m_1}^{(l)} n_{\tilde{m}_1} + \sum_{m_2=v_1-k+1}^{M} \mathbf{s}_{c,m_2}^{(l)} \big(\sum_{l=1}^{L} \mathbf{s}_{\tilde{m}_2}^{(l)} \tilde{h}^{(l)} \eta^{(l)} + n_{\tilde{m}_2} \big) \right] \\
&\overset{\text{II}}{=} \frac{1}{\sqrt{M}} \left[\sum_{m=1}^{M} \tilde{n}_m + \tilde{h}^{(l)} A_{c,k}^{(l)} \eta^{(l)} + \sum_{\substack{\tilde{l}=1 \\ \tilde{l}\neq l}}^{L-1} \tilde{h}^{(\tilde{l})} A_{c,k}^{(\tilde{l})} \eta^{(\tilde{l})} \right] \\
&= \frac{1}{\sqrt{M}} \big(A_{c,k}^{(l)} \tilde{h}^{(l)} \eta^{(l)} + \sum_{\substack{\tilde{l}=1 \\ \tilde{l}\neq l}}^{L-1} \tilde{h}^{(\tilde{l})} A_{c,k}^{(\tilde{l})} \eta^{(\tilde{l})} + \tilde{n} \big),
\end{aligned} \tag{10}$$

where $\tilde{m}_1 = m_1 + k, \tilde{m}_2 = m_2 + k$, $\tilde{n} = \sum_{m=1}^{M} \tilde{n}_m$, and

$$A_{c,k}^{(d)} = \begin{cases} \sum\limits_{m_2=v_1-k+1}^{M} \mathbf{s}_{c,m_2}^{(l)} \mathbf{s}_{\tilde{m}_2}^{(d)}, & \text{for } k < v_1, \\ \sum\limits_{m_2=1}^{M} \mathbf{s}_{c,m_2}^{(l)} \mathbf{s}_{\tilde{m}_2}^{(d)}, & \text{for } k = v_1, \\ \sum\limits_{m_2=1}^{M+v_1-k} \mathbf{s}_{c,m_2}^{(l)} \mathbf{s}_{\tilde{m}_2}^{(d)}, & \text{for } k > v_1, \end{cases} \tag{11}$$

with $d \in \{l, \tilde{l}\}$. Note that in step I, we isolate pure noise terms from the ones of the received signal and, without loss of generality, we assume $v_1 < M$. In step II, we further isolate all of the noise terms from the ones of the pure received signal samples, and the main signal of interest from other interference terms. Consequently, without loss of generality and in light of (6) and (10), we rewrite (7) as

$$\begin{aligned}
D^{(l)} &= \frac{1}{M} \max \left(\left| A_{c,k}^{(l)} \tilde{h}^{(l)} \eta^{(l)} + \sum_{\substack{\tilde{l}=1 \\ \tilde{l}\neq l}}^{L-1} \tilde{h}^{(\tilde{l})} A_{c,k}^{(\tilde{l})} \eta^{(\tilde{l})} + \tilde{n} \right|^2 \right) \\
&\overset{\text{I}}{\approx} \frac{1}{M} \max \left(\left| A_{c,k}^{(l)} \tilde{h}^{(l)} \eta^{(l)} + \sum_{\substack{\tilde{l}=1 \\ \tilde{l}\neq l}}^{L-1} \tilde{h}^{(\tilde{l})} A_{c,k}^{(\tilde{l})} \eta^{(\tilde{l})} \right|^2 \right),
\end{aligned} \tag{12}$$

where, in step I, we ignored the noise effect for large values of $N^{(l)}$ and/or $P\beta^{(l)}$, as the received signal variance is much larger than the one of the noise, as will be shown later in this subsection. As seen from (12), it is very difficult to obtain the exact distribution of $D^{(l)}$[8]. Therefore, in what follows, we consider the single ($L=1$) and two ($L=2$) RISs cases to demonstrate the performance metrics of our proposed RIS-ID scheme.

1) Single RIS case ($L=1$): The probability that the ($l=1$) - th RIS is falsely detected (declared to be reachable) can be obtained from (8), as

$$P_F^{(1)} = P(D^{(1)} > r^{(1)}), \tag{13}$$

where if there is no reachable RIS, we obtain the received signal as given in (3). Note that, for $y_m = n_m$, $\mathbf{s}_{c,m}^{(1)} \in \{-1, 1\}$,

[7] In practice, for a given RISs deployment environment, these probabilities can be obtained empirically from real-world measurements.

[8] While not explicitly addressed in this study, the distribution of $D^{(l)}$ for general L can be obtained through numerical methods.

and considering the random distribution symmetry, we have $d_{c,k}^{(1)} \sim \mathcal{CN}(0, \sigma_n^2)$, as it is a normalized sum of independent and identically distributed (i.i.d.) complex Gaussian random variables (CGRVs). Therefore, we obtain $|d_{c,k}^{(1)}|^2 \sim \chi^2(2)$, where $\chi^2(z)$ denotes the chi-square random distribution with z degrees of freedom. Due to the overlap in the summed elements of different $d_{c,k}^{(1)}$'s, they are dependent RVs, which makes it very challenging to obtain the exact distribution of $D^{(1)}$. Nevertheless, the right-tail probability of $D^{(1)}$ in (13) can be upper-bounded as [17]

$$\begin{aligned} P_F^{(1)} &\leq \min\{1, (v_1+v_2+1)M(1-F(r^{(1)}))\} \\ &= \min\{1, (v_1+v_2+1)M\exp(-r^{(1)}/\sigma_n^2)\}, \end{aligned} \tag{14}$$

where $F(r^{(1)}) = 1 - e^{-r^{(1)}/\sigma_n^2}$ is the cumulative distribution function (CDF) of $|d_{c,k}^{(1)}|^2$ and $(v_1+v_2+1)M$ is the number of arguments (dependent χ^2 RVs) of the $\max$ function in (6), obtained according to (5).

As seen from (14), the false detection probability is inversely proportional to the threshold value $r^{(1)}$, while it is directly proportional to the number of collected extra samples (v_1+v_2), the sequence length M, and the noise variance σ_n^2. Accordingly, there is no effect of the reflected signal's characteristics or UE-RIS channel on the false detection of an RIS.

2) Two RISs case ($L=2$): From (8), for $L=2$, $P_F^{(l)}$ can be written as

$$P_F^{(l)} = \frac{1}{2}\big(P\big(D^{(l)} > r^{(l)}|\eta^{(\tilde{l})}=0\big) + P\big(D^{(l)} > r^{(l)}|\eta^{(\tilde{l})}=1\big)\big), \tag{15}$$

where, $P(D^{(l)} > r^{(l)}|\eta^{(\tilde{l})}=0)$ is given in (14). To derive the second probability, we note that for $\eta^{(\tilde{l})}=1, \eta^{(l)}=0$ and using (12), we obtain

$$\begin{aligned} D^{(l)} &\approx \frac{1}{M}\max\left(\left|A_{c,k}^{(\tilde{l})}\tilde{h}^{(\tilde{l})}\right|^2\right) = \frac{|\tilde{h}^{(\tilde{l})}|^2}{M}\max\left(\left|A_{c,k}^{(\tilde{l})}\right|^2\right) \\ &= H^{(\tilde{l})}\left|A_{\hat{c},\hat{k}}^{(\tilde{l})}\right|^2, \end{aligned} \tag{16}$$

where $H^{(\tilde{l})} = \frac{|\tilde{h}^{(\tilde{l})}|^2}{M}$.

To obtain the distribution of $H^{(\tilde{l})}$, first, we note that by expressing the channel component as $h_i^{(\tilde{l})} = a + jb$, where $a, b \sim \mathcal{N}(0, 0.5P\beta^{(\tilde{l})})$, we obtain $(h_i^{(\tilde{l})})^2 = a^2 - b^2 + 2jab$ having a complicated distribution corresponding to the complex difference of two chi-square RVs and a product of two Gaussian RVs. In addition, due to the spatial correlation between RIS elements, we have $h_i^{(\tilde{l})}$'s are non-independent R.Vs, making it challenging to obtain the exact distribution of the sum $\tilde{h}^{(\tilde{l})} = \sum_{i=1}^{N^{(\tilde{l})}}(h_i^{(\tilde{l})})^2$. Therefore, to make the derivations more tractable, we first ignore the spatial correlations between RIS elements, $\mathbf{R} = \mathbb{I}_{N^{(\tilde{l})}}$; and thus, $(h_i^{(\tilde{l})})^2$'s are i.i.d. RVs.[9]. In light of this, we use the central limit theorem (CLT) to approximate the distribution of the overall sum $\tilde{h}^{(\tilde{l})} = \sum_{i=1}^{N^{(\tilde{l})}}(h_i^{(\tilde{l})})^2$ to the CG distribution, irrespective of the distribution of its individual elements. Accordingly, we obtain $\tilde{h}^{(\tilde{l})} \sim \mathcal{CN}(0, 2N^{(\tilde{l})}P\beta^{(\tilde{l})})$ as $N^{(\tilde{l})} \to \infty$, where $\mathrm{E}[(h_i^{(\tilde{l})})^2] = 0$ and $\mathrm{VAR}[(h_i^{(\tilde{l})})^2] = 2P\beta^{(\tilde{l})}$, with $\mathrm{E}[\cdot]$ and $\mathrm{VAR}[\cdot]$ denoting the statistical expectation and variance operators, respectively. Therefore, $H^{(\tilde{l})} = |\tilde{h}^{(\tilde{l})}|^2/M$ is a chi-square RV with two degrees of freedom ($\chi^2(2)$). Furthermore, due to the random cyclic shift (c), $\left|A_{\hat{c},\hat{k}}^{(\tilde{l})}\right|^2$ becomes a discrete RV with finite number of distinct values. Consequently, $D^{(l)}$ corresponds to the product of a continuous and discrete RVs and its right-tail probability can be found as

$$\begin{aligned} &P(D^{(l)} > r^{(l)}|\eta^{(\tilde{l})}=1) = 1 - P(D^{(l)} < r^{(l)}|\eta^{(\tilde{l})}=1) \\ &\approx 1 - P(H^{(\tilde{l})}|A_{\hat{c},\hat{k}}^{(\tilde{l})}|^2 < r) \\ &= 1 - \sum_{w=1}^{W} P(H^{(\tilde{l})}a_w^{(\tilde{l})} < r \,||A_{\hat{c},\hat{k}}^{(\tilde{l})}|^2 = a_w^{(\tilde{l})})P(|A_{\hat{c},\hat{k}}^{(\tilde{l})}|^2 = a_w^{(\tilde{l})}) \\ &\overset{\text{I}}{=} 1 - \sum_{w=1}^{W}\left(1 - \exp\left(\frac{-r^{(l)}}{\frac{2N^{(\tilde{l})}P\beta^{(\tilde{l})}a_w^{(\tilde{l})}}{M}}\right)\right)P(|A_{\hat{c},\hat{k}}^{(\tilde{l})}|^2 = a_w^{(\tilde{l})}), \end{aligned} \tag{17}$$

where, $0 \leq a_w^{(\tilde{l})} \leq M^2$ is an integer. In step I, we substituted the CDF of the chi-square RV $H^{(\tilde{l})}a_w^{(l)}$ [18]. Finally, the probability given in (15) can be written in terms of (14) and (17) as

$$\begin{aligned} P_F^{(l)} &\approx \frac{1}{2}\min\{1, (v_1+v_2+1)M\exp(-r^{(l)}/\sigma_n^2)\} \\ &\quad + \frac{1}{2} - \frac{1}{2}\sum_{w=1}^{W}\left(1 - \exp\left(\frac{-r^{(l)}}{\frac{2N^{(\tilde{l})}P\beta^{(\tilde{l})}a_w^{(\tilde{l})}}{M}}\right)\right) \\ &\quad \times P(|A_{\hat{c},\hat{k}}^{(\tilde{l})}|^2 = a_w^{(\tilde{l})}) \\ &\overset{\text{I}}{\approx} \frac{1}{2} - \frac{1}{2}\sum_{w=1}^{W}\left(1 - \exp\left(\frac{-r^{(l)}}{\frac{2N^{(\tilde{l})}P\beta^{(\tilde{l})}a_w^{(\tilde{l})}}{M}}\right)\right) \\ &\quad \times P(|A_{\hat{c},\hat{k}}^{(\tilde{l})}|^2 = a_w^{(\tilde{l})}), \end{aligned} \tag{18}$$

where, in step I, we considered that the second probability (associated with the event where the $\tilde{l}$-th RIS is reachable, $\eta^{(\tilde{l})}=1$) is dominating the first one associated with the noise samples only ($\eta^{(\tilde{l})}=0$), due to large $P\beta^{(\tilde{l})}$ and/or $N^{(\tilde{l})}$ values.

B. Miss-Detection Probability

By following the same derivation steps given in Section III-A, the miss detection probability can be obtained, by using (8) and considering the right-tail probability (switching the inequality sign), as

$$\begin{aligned} P_{miss}^{(l)} &= P(D^{(l)} < r^{(l)}|\eta^{(l)}=1) \\ &\overset{\text{III}}{=} \left(\frac{1}{2}\right)^{L-1}\sum_{w=1}^{2^{L-1}} P\left(D^{(l)} < r^{(l)}\,\middle|\bigcap_{\substack{\tilde{l}=1 \\ \tilde{l}\neq l}}^{L-1}(\eta^{(\tilde{l})} = \eta_w^{(\tilde{l})})\right), \end{aligned} \tag{19}$$

where, w is given in Section III-A.

In what follows, we consider the miss-detection probability of the two cases: $L=1$ and $L=2$.

1) Single RIS case ($L=1$): Considering the $(l=1)$-th RIS as the only reachable RIS and using (19), the probability of miss-detecting it (declaring it unreachable) can be given as

$$P_{miss}^{(1)} = P(D^{(1)} < r^{(1)}). \tag{20}$$

[9]We show later in simulation results that the effect of spatial correlation is insignificant, validating our i.i.d. approximation.

Note that, when $\eta^{(1)}=1$ and using (12), we have

$$D^{(1)} \approx \frac{1}{M}\max\left(\left|A_{c,k}^{(1)}\tilde{h}^{(1)}\right|^2\right) = \frac{|\tilde{h}^{(1)}|^2}{M}\max\left(\left|A_{c,k}^{(1)}\right|^2\right) = \frac{|\tilde{h}^{(1)}|^2|A_{\hat{c},\hat{k}}^{(1)}|^2}{M} \overset{\text{I}}{=} |\sqrt{M}\tilde{h}^{(1)}|^2, \tag{21}$$

where $D^{(1)} \sim \chi^2(2)$ as shown previously. In step I, we considered the fact that for the optimal parameters $\hat{c}$ and $\hat{k}$, we have perfect alignment between $\mathbf{s}_{c,m_2}^{(1)}$ and $\mathbf{s}_{\tilde{m}_2}^{(1)}$ with $A_{\hat{c},\hat{k}}^{(1)}=M$ corresponding to the maximum correlation amplitude. Consequently, $P_{miss}^{(1)}$ corresponds to the CDF of $D^{(1)}$ and can be given as

$$P_{miss}^{(1)} \approx 1-\exp\left(\frac{-r^{(1)}}{2N^{(1)}P\beta^{(1)}M}\right). \tag{22}$$

As in the $P_F^{(1)}$, $P_{miss}^{(1)}$ is directly affected by the threshold setting; however, it is directly proportional to $r^{(l)}$ and inversely to $M, N^{(1)}$ P and $\beta^{(1)}$.

2) Two RISs case ($L=2$): Considering the l-th RIS be reachable ($\eta^{(l)}=1$) and using (19), we have

$$P_{miss}^{(l)} = \frac{1}{2}\big(P\big(D^{(l)}<r^{(l)}|\eta^{(\tilde{l})}=0\big)+P\big(D^{(l)}<r^{(l)}|\eta^{(\tilde{l})}=1\big)\big), \tag{23}$$

where the first probability is given in (22). To obtain the second probability, we note that, for $\eta^{(l)}=\eta^{(\tilde{l})}=1$ and using (12), we obtain

$$\begin{aligned} D^{(l)} &\approx \frac{1}{M}\max\left(\left|A_{c,k}^{(l)}\tilde{h}^{(l)}+A_{c,k}^{(\tilde{l})}\tilde{h}^{(\tilde{l})}\right|^2\right) \\ &\overset{\text{I}}{\leq} \frac{1}{M}\max\left(\left(\left|A_{c,k}^{(l)}\tilde{h}^{(l)}\right|+\left|A_{c,k}^{(\tilde{l})}P\tilde{h}^{(\tilde{l})}\right|\right)^2\right) \\ &\overset{\text{II}}{\leq} \frac{1}{M}\big(A_{\hat{c},\hat{k}}^{(l)}\left|\tilde{h}^{(l)}\right|+\tilde{A}^{(\tilde{l})}\left|\tilde{h}^{(\tilde{l})}\right|\big)^2 \\ &\overset{\text{III}}{=} \frac{1}{M}\big(M\left|\tilde{h}^{(l)}\right|+\tilde{A}^{(\tilde{l})}\left|\tilde{h}^{(\tilde{l})}\right|\big)^2, \end{aligned} \tag{24}$$

where, in step I, we used $|a+b|^2=|a|^2+|b|^2+2\mathbb{R}\{ab^*\}\leq |a|^2+|b|^2+2|a||b|=(|a|+|b|)^2$. Furthermore, in step II, we considered the upper bounds for the two terms, $A_{c,k}^{(l)}\leq A_{\hat{c},\hat{k}}$ and $A_{c,k}^{(\tilde{l})}\leq \tilde{A}^{(\tilde{l})}, \forall c,k$, where we obtain $\tilde{A}^{(\tilde{l})}$ empirically through simulations, while, in step III, we set $A_{\hat{c},\hat{k}}=M$ denoting the maximum possible correlation amplitude. Consequently, using (24), we obtain

$$\begin{aligned} &P(D^{(l)}\leq r^{(l)}|\eta^{(\tilde{l})}=1) \geq P\big(\frac{1}{M}\big(M|\tilde{h}^{(l)}|+\tilde{A}^{(\tilde{l})}|\tilde{h}^{(\tilde{l})}|\big)^2\leq r^{(l)}\big) \\ &= P\left(\left|\frac{M\tilde{h}^{(l)}}{\sqrt{M}}\right|+\left|\frac{\tilde{A}^{(l)}\tilde{h}^{(\tilde{l})}}{\sqrt{M}}\right|\leq\sqrt{r^{(l)}}\right) \overset{\text{I}}{=} P(R\leq\sqrt{r^{(l)}}) \\ &\overset{\text{II}}{=} \frac{1}{2}-\int_0^\infty \frac{\Im\{e^{jw\sqrt{r^{(l)}}}\Psi_R(w)\}}{w\pi}dw, \end{aligned} \tag{25}$$

where in step I, we have $R=R_1+R_2$ with $R_1=\left|\frac{M\tilde{h}^{(l)}}{\sqrt{M}}\right|$ and $R_2=\left|\frac{\tilde{A}^{(l)}\tilde{h}^{(\tilde{l})}}{\sqrt{M}}\right|$ are Rayleigh distributed RVs. In step II, we utilize Gil-Pelaez's inversion formula to obtain the CDF of R using its characteristic function (CF) [19], which is given as

$$\Psi_R(w)=\Psi_{R_1}(w)\Psi_{R_2}(w), \tag{26}$$

where $\Psi_{R_1}(w)$ and $\Psi_{R_2}(w)$ are the CFs of R_1 and R_2, respectively, and for $i=1,2$, we have

$$\Psi_{R_i}(w)=e^{-\frac{w^2\sigma_i^2}{2}}\sum_{k=0}^{\infty}\frac{\left(\frac{1}{2}w^2\sigma_i^2\right)^k}{(2k-1)!}+j\sqrt{\frac{\pi}{2}}w\sigma_i e^{-\frac{w^2\sigma_i^2}{2}}, \tag{27}$$

with $\sigma_1=\sqrt{MN^{(l)}P\beta^{(l)}}$ and $\sigma_2=\sqrt{\frac{\tilde{A}^{(\tilde{l})}}{M}N^{(\tilde{l})}P\beta^{(\tilde{l})}}$. Finally, substituting (22) and (25) in (23), we get

$$P_{miss}^{(l)} \geq \frac{3}{2}-\exp\left(\frac{-r^{(l)}}{2N^{(l)}P\beta^{(l)}M}\right)-\int_0^\infty\frac{\Im\{e^{jw\sqrt{r^{(l)}}}\Psi_R(w)\}}{w\pi}dw. \tag{28}$$

C. Detection Threshold Setting

Here, in light of the previous mathematical analyses, we discuss the threshold setting at the UE side to achieve a predetermined performance level.

1) Single RIS case ($L=1$): For the UE to set the detection threshold, first, the required false detection probability $P_F^{(l)}$ value needs to be set as a given design parameter. Furthermore, the noise variance σ_n^2 needs to be obtained using actual signal measurements at the automatic gain control (AGC) output or as a constant value from its data sheet [14]. Using the obtained σ_n^2 and the required $P_F^{(l)}$, the detection threshold can be obtained from (14). It is worth noting that, as can be seen from (14) and (22), the detection threshold $r^{(l)}$ can not be set to both minimize $P_F^{(l)}$ and $P_{miss}^{(l)}$. Furthermore, $r^{(l)}$ and sequence length M are the only parameters to control $P_F^{(l)}$, while $N^{(l)}$ and P can also be used in the case of $P_{miss}^{(l)}$, as follows.

Having the threshold and sequence length set and in order to obtain the required miss-detection probability, we solve (22) for $N^{(l)}$ to obtain

$$\bar{N}^{(l)}=\frac{-r^{(l)}}{2P\beta^{(l)}M\ln(1-P_{miss}^{(l)})}, \tag{29}$$

where $\bar{N}^{(l)}$ corresponds to the required RIS size to obtain the targeted $P_{miss}^{(l)}$. Likewise, (22) can be solved for P to obtain the required transmit power for the targeted $P_{miss}^{(l)}$.

2) Two RISs case ($L=2$): In the two RISs case, as seen from (18) and (28), all parameters affect both $P_F^{(l)}$ and $P_{miss}^{(l)}$. Specifically, $P_F^{(l)}$ is directly proportional to P and $N^{(l)}$, and inversely to $r^{(l)}$ and M. On the other side, $P_{miss}^{(l)}$ is directly proportional to $r^{(l)}$ and inversely to P, $N^{(l)}$, and M. Furthermore, it can be noted that $P_F^{(l)}$ and $P_{miss}^{(l)}$ exhibit an opposite behavior in response to the change in P, $N^{(l)}$, and $r^{(l)}$, while they have a similar inverse proportion to M. Consequently, in order to set the detection threshold, the two functions ($P_F^{(l)}$ and $P_{miss}^{(l)}$) can be plotted (y-axis) against a range of threshold values (x-axis) to select the value that satisfies both $P_F^{(l)}$ and $P_{miss}^{(l)}$ requirements, as will be shown in Section IV.

IV. Simulation Results

In this section, we provide extensive computer simulations to assess the performance of the proposed RIS-ID scheme, focusing on evaluating two critical performance metrics: false detection and miss-detection probabilities. Without loss of generality, as a BSeq, Walsh-Hadamard codes are used to represent RISs IDs in the shared look-up table. This is because these codes are known for their widespread use in

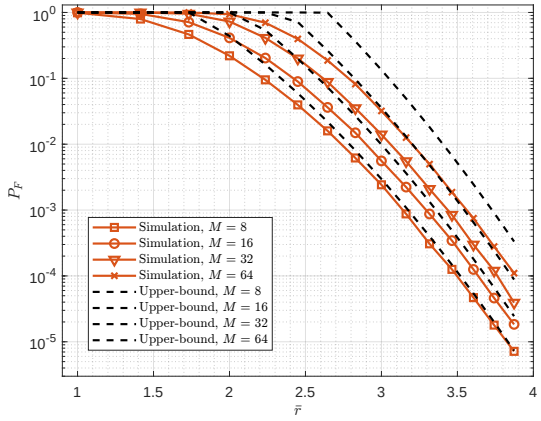

Fig. 2. The impact of the sequence length M on the false detection probability when $L = 1$.

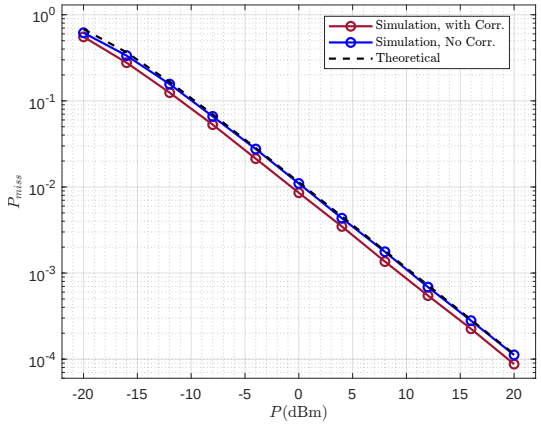

Fig. 3. Miss-detection probability with and without correlation, for $L = 1$.

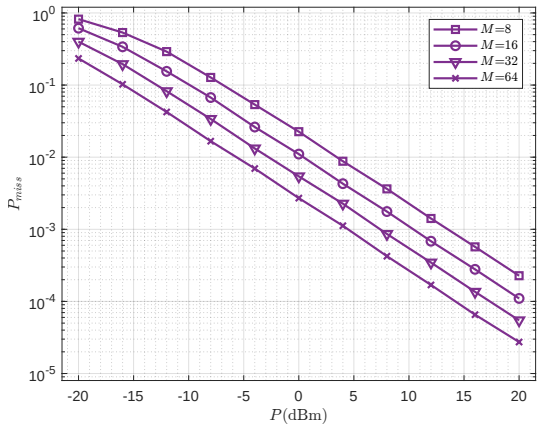

Fig. 4. The impact of M on the miss-detection probability when $L = 1$.

code division multiple access (CDMA) applications owing to their orthogonality property, which aligns with our purpose of distinguishing multiple RISs simultaneously. Furthermore, we assume identical RIS size and UE-RIS distance (path gain) for different RISs; therefore, the index l is omitted from N, β, and r. Furthermore, we consider an operating bandwidth (BW) of 20 MHz, the number of extra collected samples $v_1 + v_2 = 0.25M$ where M is the sequence length and $v_1 \in \mathcal{U}\{1, 2, \ldots, 0.25M\}$, and $\sigma_n^2 = -174$ dBm $+10\log_{10}(\text{BW}) = -101$ dBm [20].

The overall UE-RIS-UE path gain, β, is calculated as [21]

$$\beta = \frac{\lambda^4}{256\pi^2 (d_{\text{UR}})^4}, \tag{30}$$

where λ represents the wavelength corresponding to $f_c = 1.8$ GHz, d_{UR} is the RIS-UE distance, which is assumed to be 10 meters for all RISs.

The spatial correlation matrix $\mathbf{R}$ is constructed based on the model proposed in [16], where the RIS elements are spaced at intervals of $\lambda/2$. Accordingly, the spatial correlation between the w-th and $\tilde{w}$-th RIS elements is expressed as

$$[\mathbf{R}]_{w,\tilde{w}} = \text{sinc}\left(\frac{2\left\|\mathbf{u}_w - \mathbf{u}_{\tilde{w}}\right\|}{\lambda}\right), \; w, \tilde{w} \in \{1, 2, \ldots, N\}, \tag{31}$$

where $\text{sinc}(\tau) = \sin(\pi\tau)/(\pi\tau)$ is the sinc function, $\mathbf{u}_k = [0, \quad i_H(w)d_H, i_V(w)d_V]^T$ is the spatial vector representing the position of the w-th RIS element, with $i_H(w) = \text{mod}\,(w-1, N_H)$, $i_V(w) = \lfloor (w-1)/N_H \rfloor$, d_H and d_V correspond the horizontal index, vertical index, width, and length of the w-th element, respectively. Here, N_H denotes the number of RIS elements per row. In what follows, we provide simulation results for the two cases ($L = 1$ and $L = 2$), separately.

A. Single RIS Case

In this subsection, we consider a single potentially reachable RIS in the environment where the UE tries to detect its presence and uniquely identify it. Here, we set $N = 64$ and $M = 16$, unless otherwise stated.

In Fig. 2, we investigate the influence of the sequence length M on the false detection probability P_F, where the x-axis indicates the normalized threshold value, $\bar{r} = (r/\sigma_n^2)^{1/2}$. It can be seen that the theoretical upper bound obtained in (14) is tight, where it converges to the simulation curve at higher values of $\bar{r}$ and lower values of M. Furthermore, increasing M increases P_F, as more noise samples are involved in the correlation process and, thus, more arguments in (6) to select from. For instance, when $\bar{r}$ is set to 3, doubling M leads to a 2.2-fold increase in the P_F.

Fig. 3 illustrates the P_{miss} for the proposed scheme in the presence and absence of the spatial correlation between RIS elements. Here, $\bar{r}$ is set to 3, which upper-bounds P_F to 10^{-2} as shown in Fig. 2. It can be seen that the spatial correlation among RIS elements does not significantly impact the performance of the proposed scheme where P_{miss} is only around 1.2 times higher when considering it. Furthermore, it can be noted that the simulation curve for the uncorrelated scenario aligns closely with the theoretical one obtained under the no-correlation assumption, demonstrating the validity of our derivations in Section III.

In Fig. 4, we show the impact of the sequence length M on the miss-detection probability P_{miss} for $\bar{r} = 3$. It can be seen that increasing M decreases the P_{miss}, where doubling M yields approximately 3 dB gain for the required P to achieve $P_{miss} = 10^{-3}$. This behavior can be verified from (22), where P_{miss} inversely proportional to M. It is worth noting that while the increase in M leads to an improvement for the P_{miss}, it concurrently results in performance degradation for

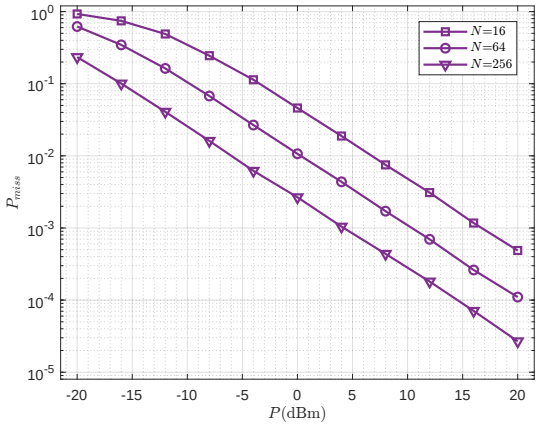

Fig. 5. The impact of the RIS size on the miss-detection probability when $L = 1$.

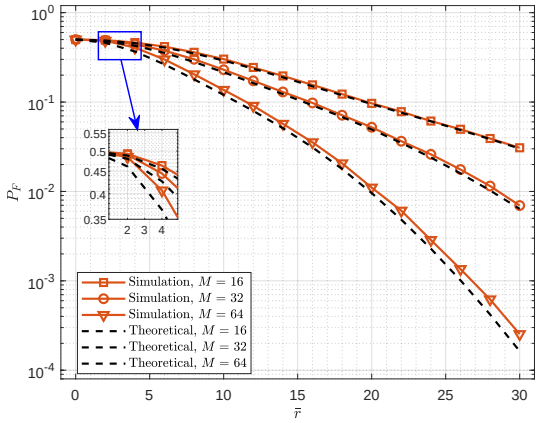

Fig. 6. The impact of M on the false detection probability when $L = 2$.

the P_F, as seen in Fig. 2. Therefore, when determining the optimal value of M, it is imperative to consider the required values for P_F and P_{miss} together, as discussed in Section III-C.

In Fig. 5, we examine the P_{miss} for various RIS sizes when $\bar{r} = 3$. It can be seen that as N increases, there is an improvement in the P_{miss}. For instance, at a P_{miss} value of 10^{-3}, around 6 dB gain is achieved for the required P by quadrupling N. This behavior can be verified from (22), where P_{miss} is inversely proportional to N.

B. Two RISs Case

In this case, we consider two potentially reachable RISs, denoted as RIS 1 and RIS 2, where the UE tries to identify reachable ones. Throughout this subsection, unless explicitly stated, we have $M = 32$ and $N = 256$, while P_F and P_{miss} probabilities are obtained for the first RIS ($l = 1$). In what follows, we first investigate the effects of certain parameters (such as M and N) on P_F and P_{miss}. Subsequently, we present an illustration chart of the system's overall performance, encompassing performance metrics for both RISs.

In Fig. 6, we show the effect of the sequence length M on P_F when P is set to 10 dBm. First, we observe that simulation curves closely match with the theoretical ones obtained using (18). It is noteworthy that the alignment between simulation

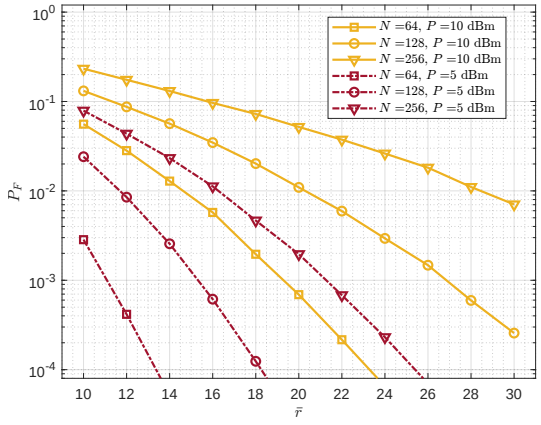

Fig. 7. The false detection probability for $L = 2$, varying with different N and P values.

and theoretical curves is more evident when employing lower values of M. This is expected as the variance of the noise term, $M\sigma_n^2$, decreases proportionally with M, making our approximation in ignoring the noise term in deriving (12) more accurate. It can also be seen that, contrary to the $L = 1$ case, increasing M decreases P_F. Specifically, when $\bar{r}$ is set to 20, increasing M from 16 to 32 reduces P_F by a factor of 2. This behavior can be verified from (18) where P_F is inversely proportional to M. Moreover, it is valuable to note that P_F observed in Fig. 6 is much higher than the one in Fig 2. For instance, when $M = 32$ and $\bar{r} = 3$, P_F in Fig. 6 is around 0.5 while P_F in Fig. 2 is around 0.01. This difference validates the accuracy of our assumption to ignore the first probability term in (15) (corresponds to P_F in Fig. 2) to approximate P_F (in Fig. 6) as in (18).

In Fig. 7, P_F is evaluated when the RIS size N and UE transmit power P change. It is clearly seen that higher values of N lead to an increase in P_F. As an example, with P is set to 10 dBm and $\bar{r}$ is set to 18, P_F takes on the values of 0.002, 0.020, and 0.073 for $N = 64$, $N = 128$, and $N = 256$, respectively. Furthermore, it is evident from Fig. 7 that increasing P results in an increase in P_F, where for $N = 256$ and $\bar{r} = 18$, P_F takes on the values 0.005 and 0.073, for $P = 5$ dBm and $P = 10$ dBm, respectively. It should be noted that the performance degradation of P_F with the increment in P and/or N arises from the fact that, as P and/or N increases, the power of the received signal reflected from the $\tilde{l}$-th RIS increases, increasing the correlation amplitude in (7). This behavior can also be verified from (18), where P_F is proportional to P and N.

Fig. 8 shows P_{miss} versus normalized threshold $\bar{r}$, considering different sequence lengths M, with P is set to 0 dBm. First, it can be seen that the theoretical lower-bound derived in (28) closely aligns with the simulation results, where increasing M and $\bar{r}$ values makes this alignment more pronounced. Also, we note that increasing M yields improvement in the P_{miss} where doubling M corresponds to approximately a two-fold reduction in P_{miss}. This note is consistent with the inverse proportional relationship of P_{miss} and M expressed in (28). Moreover, increasing $\bar{r}$ decreases P_{miss}, for instance, when $M = 32$, P_{miss} is 0.057, 0.132, 0.256 for $\bar{r} = 20$, $\bar{r} = 30$, and $\bar{r} = 40$, respectively. This behavior can be verified from

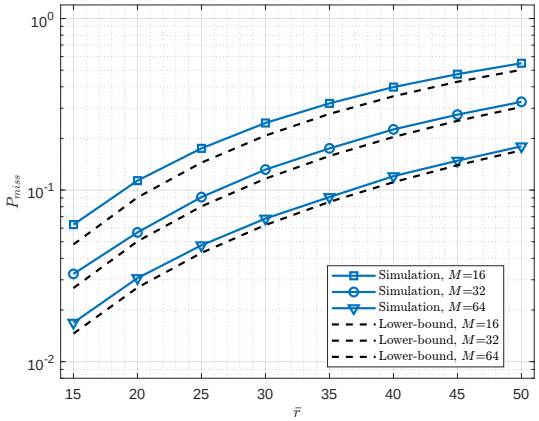

Fig. 8. The impact of M on the miss-detection probability when $L = 2$.

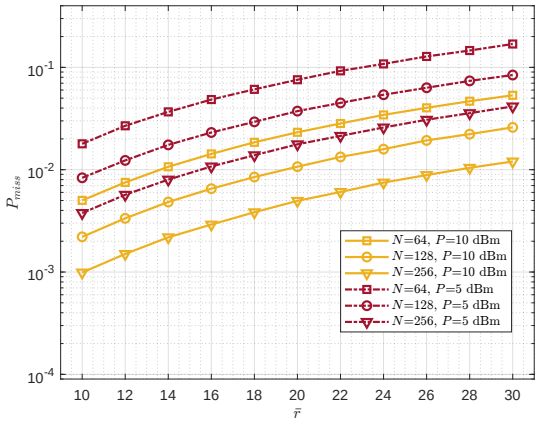

Fig. 9. The miss-detection probability for $L = 2$, varying with different N and P values.

(28), where P_{miss} is proportional to r.

In Fig. 9, we examine the impact of the RIS size N and UE transmit power P on P_{miss}. It can be observed that, as in the single RIS case, increasing N and/or P both decreases P_{miss}. For example, with $P = 10$ dBm and $\bar{r} = 20$, P_{miss} is halved by doubling N. Likewise, with $N = 256$ and $\bar{r} = 20$, increasing P from 5 dBm to 10 dBm decreases P_{miss} from 0.0178 to 0.005. Our observations from Fig. 9 can be verified from (28), where P_{miss} is inversely proportional to N and P.

In Fig. 10, we explore the performance trade-off in terms of the probabilities P_{miss} and P_F. Differing from previous figures within this section, we incorporate P_{miss} and P_{F} for both RIS 1 and RIS 2. Initially, we see that as $\bar{r}$ increases, P_F decreases while P_{miss} increases. Moreover, as depicted in Fig. 10, different P_F and P_{miss} values are noticed for different RISs, although they share the same simulation parameters. This discrepancy arises from the different realizations of the discrete RV $|A^{(\tilde{l})}_{\hat{c},\hat{k}}|$ in (18) for different RISs. Furthermore, we observe that the gap between P_{miss} curves is much narrower than that in P_F curves. The reason is that the dominating term in (18) is the part including $|A^{(\tilde{l})}_{\hat{c},\hat{k}}|$, while the dominating term in (28), common for both RISs, does not involve $A^{(\tilde{l})}_{\hat{c},\hat{k}}$.

Fig. 11 summarizes the results in the previous figures in a different illustration approach, using confusion matrix charts

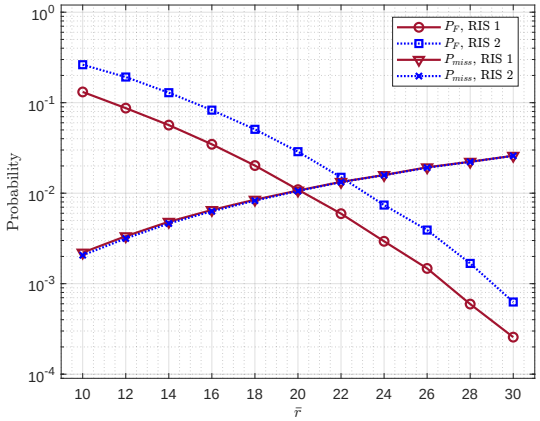

Fig. 10. The impact of threshold setting on P_F and P_{miss}, for $P = 10$ dBm, $M = 32$, $N = 128$, and $L = 2$.

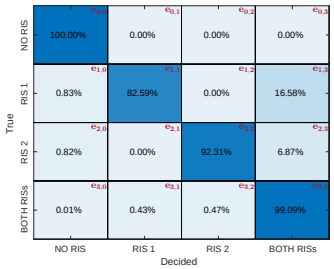

(a) $\bar{r} = 16$.

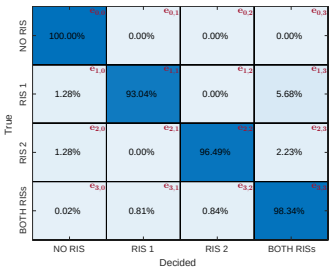

(b) $\bar{r} = 20$.

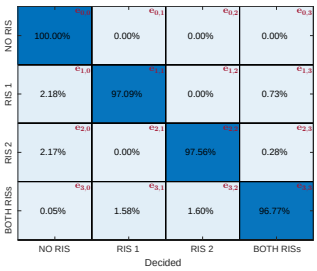

(c) $\bar{r} = 26$.

Fig. 11. Performance evaluation of the the proposed RIS-ID scheme using a confusion matrix illustrating the reachability states of RISs for $L = 2$, $P = 10$ dBm, $M = 32$ and $N = 128$, . The rows and columns represent the true and decided reachability states, respectively, showcasing potential outcomes: "NO RIS" ($\eta^{(1)}, \eta^{(2)} = 0$), "RIS 1"($\eta^{(1)} = 1, \eta^{(2)} = 0$), "RIS 2" ($\eta^{(1)} = 0, \eta^{(2)} = 1$), and "BOTH RISs" ($\eta^{(1)}, \eta^{(2)} = 1$).

for comprehensive comparisons. Here, we provide simulations of 10^7 random realizations to generate these charts. In each realization, the reachability states of RISs are randomly set with equal probabilities, $P(\eta^{(l)} = 0) = P(\eta^{(l)} = 1), \forall l$. Then, the proposed RIS-ID scheme is used to decide which RISs are reachable by the UE and which are not. Entries of the confusion matrix are denoted by $e_{i,j}$ for $i, j = 0, \ldots, 3$, arranged from top to bottom and left to right, as illustrated in Fig. 11. The diagonal entries of the confusion matrix indicate correct decision probabilities regarding RISs' reachability. The off-diagonal entries can be used to find miss-detection and false-detection probabilities for RISs: $P^{(1)}_{miss} = [(e_{1,0} + e_{1,2})/2 + (e_{3,0} + e_{3,2})/2]$, $P^{(2)}_{miss} = [(e_{2,0} + e_{2,1})/2 + (e_{3,0} + e_{3,1})/2]$, $P^{(1)}_{F} = [(e_{0,1} + e_{0,3})/2 + (e_{2,1} + e_{2,3})/2]$, and $P^{(2)}_{F} = [(e_{0,2} + e_{0,3})/2 + (e_{1,2} + e_{1,3})/2]$.

V. Conclusion

This study has proposed a novel RIS-ID solution to enable UEs to detect and uniquely identify reachable RISs in the surrounding environment as a first and essential step to utilize them. Furthermore, false and miss detection probabilities have been proposed as metrics to examine the performance of the proposed solution. The theoretical and simulation results clearly show the effectiveness of the proposed RIS-ID scheme when considering different system settings. As a dominant parameter, the type of the used binary sequence (its autocorrelation and orthogonality properties) determines the overall performance of the proposed scheme to detect and identify multiple RISs accurately. For future research, joint RIS-ID and passive beamforming is a problem worth investigating.

References

[1] E. Basar *et al.*, "Wireless communications through reconfigurable intelligent surfaces," *IEEE Access*, vol. 7, pp. 116 753–116 773, Aug. 2019.

[2] C. Pan *et al.*, "Reconfigurable intelligent surfaces for 6G systems: Principles, applications, and research directions," *IEEE Commun. Mag*, vol. 59, no. 6, pp. 14–20, Jun. 2021.

[3] A. Khaleel and E. Basar, "A novel NOMA solution with RIS partitioning," *IEEE J. Sel, Topics in Signal Process*, vol. 16, no. 1, pp. 70–81, Jan. 2022.

[4] ——, "Reconfigurable intelligent surface-empowered MIMO systems," *IEEE Syst. J.*, vol. 15, no. 3, pp. 4358–4366, Sep. 2021.

[5] E. Basar, "Reconfigurable intelligent surface-based index modulation: A new beyond MIMO paradigm for 6G," *IEEE Trans. Commun.*, vol. 68, no. 5, pp. 3187–3196, May 2020.

[6] H. Wymeersch *et al.*, "Radio localization and mapping with reconfigurable intelligent surfaces: Challenges, opportunities, and research directions," *IEEE Veh. Technol. Mag.*, vol. 15, no. 4, pp. 52–61, Dec. 2020.

[7] J. Hu *et al.*, "Reconfigurable intelligent surface based RF sensing: Design, optimization, and implementation," *IEEE J. Sel. Areas Commun.*, vol. 38, no. 11, pp. 2700–2716, Nov. 2020.

[8] H. Zhang *et al.*, "Channel estimation with simultaneous reflecting and sensing reconfigurable intelligent metasurfaces," in *Proc. IEEE 22nd Int. Workshop Signal Process. Adv. Wireless Commun. (SPAWC)*, Sep. 2021, pp. 536–540.

[9] R. Liu, M. Li, and A. L. Swindlehurst, "Joint beamforming and reflection design for RIS-assisted ISAC systems," in *Proc. 30th Eur. Signal Process. Conf. (EUSIPCO)*, Aug. 2022, pp. 997–1001.

[10] J. Zuo *et al.*, "Exploiting NOMA and RIS in integrated sensing and communication," *IEEE Trans. Veh. Commun.*, vol. 72, no. 10, pp. 12 941–12 955, Oct. 2023.

[11] Z. Wang, X. Mu, and Y. Liu, "STARS enabled integrated sensing and communications," *IEEE Trans. Wireless Commun.*, vol. 22, no. 10, pp. 6750–6765, Feb. 2023.

[12] C. Gaudreauand and A. Chaaban, "Localization by modulated reconfigurable intelligent surfaces," *IEEE Commun. Lett.*, vol. 26, no. 12, pp. 2904–2908, Dec. 2022.

[13] K. Keykhosravi, G. Seco-Granados, G. C. Alexandropoulos, and H. Wymeersch, "RIS-enabled self-localization: Leveraging controllable reflections with zero access points," in *Proc. IEEE Int. Conf. Commun.*, Jun. 2022, pp. 2852–2857.

[14] F. Ling, *Synchronization in digital communication systems*. Cambridge, U.K.: Cambridge Univ. Press, 2017.

[15] Y. He, H. Zhao, W. Guo, S. Shao, and Y. Tang, "A time-robust digital self-interference cancellation in full-duplex radios: Receiver design and performance analysis," *IEEE Access*, vol. 8, pp. 185 021–185 031, Oct. 2020.

[16] E. Björnson and L. Sanguinetti, "Rayleigh fading modeling and channel hardening for reconfigurable intelligent surfaces," *IEEE Wireless Commun. Lett.*, vol. 10, no. 4, pp. 830–834, Apr. 2021.

[17] T. L. Lai and H. Robbins, "A class of dependent random variables and their maxima," *Zeitschrift für Wahrscheinlichkeitstheorie und verwandte Gebiete*, vol. 42, no. 2, pp. 89–111, 1978.

[18] M. Simon, *Probability Distributions Involving Gaussian Random Variables*. New York, NY, USA: Springer, 2002.

[19] A. Mathai and S. B. Provost, *Quadratic Forms in Random Variables: Theory and Applications*. New York, NY, USA: Marcel Dekker, 1992.

[20] Y. Liu *et al.*, "RACH in self-powered NB-IoT networks: Energy availability and performance evaluation," *IEEE Trans. Commun.*, vol. 69, no. 3, pp. 1750–1764, Mar. 2021.

[21] S. W. Ellingson, "Path loss in reconfigurable intelligent surface-enabled channels," in *Proc. IEEE 32nd Annu. Int. Symp. Pers., Indoor Mobile Radio Commun. (PIMRC)*, Sep. 2021, pp. 829–835.